The International Journal of Advanced Manufacturing Technology (2019) 105:2237–2251
https://doi.org/10.1007/s00170-019-04400-y

ORIGINAL ARTICLE

Effects of tungsten inert gas (TIG) welding parameters on macrostructure, microstructure, and mechanical properties of AA6063-T5 using the controlled intermittent wire feeding method

Ario Sunar Baskoro[1] · Mohammad Azwar Amat[1] · Alfian Ibnu Pratama[1] · Gandjar Kiswanto[1] · Winarto Winarto[2]

Received: 14 December 2018 / Accepted: 6 September 2019/ Published online: 25 October 2019
© Springer-Verlag London Ltd., part of Springer Nature 2019

Abstract
This paper presents an automated or intermittent wire feeding method in tungsten inert gas (TIG) welding. The preliminary investigation shows the macrostructure, microstructure, and mechanical property effects on various welding parameters using one combination proportion of filler metal with various welding parameters. The result of microstructure has shown that the localized segregation occurred at the center area weld metal with high-density eutectic phase and energy dispersive X-ray spectroscopy (EDS) study has found that Mg content was higher compared to the outside region. Other sample microstructure shows columnar structure was formed in dilution boundaries, and it reveals that fast cooling rates happened when the filler wire was inserted. Also, microstructure on weld traverse section shows that the wavy-like structure depended on the heat input. The fracture mode shows that lack of heat input is susceptible to oxidation; therefore, the fracture tends to occur at weld metal in the brittle manner with reduced strength of more than 40%. Also this article presented the method to calculate length ratio (R_L) and the volume ratio (R_V) to estimate the minimum value of ratio under the condition of a good welded surface profile.

Keywords TIG welding · AA6063-T5 · Intermittent wire feeder method · ER5356 · Microstructure

1 Introduction

Aluminum alloys have been used in many applications such as aerospace, automotive industry, railway vehicles, bridges, ship structure, piping, auto-body parts, and part machined from plate or bar [1]. These alloys are frequently welded because they have fairly good weldability and have many attractive properties such as good formability and extrudability, recycling capabilities, corrosion resistance, high strength to weight ratio, high toughness, and low cost [2, 3]. Aluminum 6063 is one of the heat-treatable alloys that is very versatile and most widely used when medium strength is required. However, problems occurred when heat-treatable alloys are welded using fusion welding process. The phase transformation in the weld metal and softening in heat-affected zone inflict the decaying of mechanical properties [4]. In general, welding of aluminum alloys can be performed by using tungsten inert gas (TIG) or metal inert gas (MIG). However, MIG welding is not recommended for joining thin aluminum alloys due to excessive heat input that can cause distortion or melt through; therefore, TIG welding is preferred over MIG [5]. However, aluminum alloys have many disadvantage properties that are associated with TIG welding process, such as high thermal conductivity and coefficient of thermal expansion, the presence of oxide layer in the aluminum surface, solidification shrinkage, and high solubility of hydrogen and oxygen in the molten state [4]. And then, when these alloys are welded using TIG welding, they are more susceptible to solidification cracking on the fusion zone and loss of strength and ductility on the heat-affected zone (HAZ) [6]. The 6000 series of aluminum alloys containing magnesium of more than 1 up to 3% are sensitive and susceptible to solidification cracking if the filler metal used the same composition as the base metal. However, the cracking can be prevented by using the filler metal as a cladding that contains more than 3.5% magnesium (ex. ER5356) [7]. Wu and Wang [8] investigated that the use of high-magnesium fillers with

✉ Ario Sunar Baskoro
ario@eng.ui.ac.id

[1] Mechanical Engineering Department, Faculty of Engineering, Universitas Indonesia, Depok, Indonesia

[2] Metallurgical and Material Engineering Department, Faculty of Engineering, Universitas Indonesia, Depok, Indonesia

Table 1 Chemical composition of AA6063-T5 and filler wire ER-5356

AA6063	Si	Fe	Cu	Mn	Mg	Zn	Cr	Ti	Others	Al
wt. (%)	0.466	0.305	0.03	0.024	1.04	0.026	0.007	0.012	0.13	Bal.
ER5356	Si	Fe	Cu	Mn	Mg	Zn	Cr	Ti	Others	Al
wt. (%)	< 0.25	< 0.4	< 0.1	0.05–0.2	4.5–5.0	< 0.1	0.05–0.2	0.06–0.2	0.05–0.15	Bal.

content more than 3 wt% can provide better weldability. With the addition of ER5356 filler metal, the chemical composition of the weld metal might change significantly or slightly compared to the base metal depending on the dilution and significantly will enhance the variation of chemical composition, leading to the change in microstructure and mechanical properties. AA6063-T5 is often welded using TIG welding with ER5356 wire filler to maintain high-magnesium content of more than 3%. An important aspect that needs to be pay attention is when AA6063-T5 is welded autogenously, the weld is susceptible to localized corrosion attack and solidification cracking. The main factor is localized segregation of the Mg–Si solute element that affects the solidification temperature range and the interfacial surface tension between the eutectic phase and aluminum matrix. Devendranath Ramkumar et al. [9] investigated the effect of different filler metals on the hot corrosion behavior, microstructure, and localized segregation of the second phase on the weld metal. They are using the direct current source of pulse TIG and super austenitic stainless steel as their observable material.

In automatic or controlled TIG welding, the development and investigation of different types of technique used in wire feeding during TIG welding have not been interesting over the past decade. Many researchers have been interested and focused on hybrid welding such as TIG-MIG [10], TIG-CMT [11], and TIG-laser welding [12] to improve efficiency; others concentrate on the method for thick aluminum plate such as NG-GMAW [13, 14] and also joining dissimilar metal such as aluminum to steel [15]. However, few researchers are interested in exploring automation of wire feeding technique and investigating the result of mechanical properties and microstructure on the localized region in WM. Defects such as porosity also need to be considered. Many of the previous work has studied dilution level with an objective to investigate the solidification cracking and corrosion resistance that is susceptible in the fusion zone. Banovic et al. [16, 17] studied the dilution effect and microsegregation in the fusion zone between Ni-base alloy and super austenitic steel using gas tungsten arc welding (GTAW). They are observing the dilution level by varying the welding parameters over a full range of dilution level to provide guidelines for controlling upon the weld metal composition. Ahn et al. [18] studied the effect of dilution on Iconel 625 and 718 with Nimonic 80A using plasma transferred arc welding (PTAW). They investigated the solidification cracking susceptibility by observing microstructural examination and thermal analysis. Pickin et al. [19] studied the characteristic of dilution of Al–Cu–Mg alloy with Al–Cu filler wire using cold metal transfer (CMT) process for controlling low dilution cladding to obtain a layer wherein the composition will get less susceptible solidification cracking. Miná et al. [20] studied the dilution effect on Inconel 686 using the TIG process with cold wire. They investigate the microstructure in the fusion zone based on chemical composition, XRD analysis, and optical emission spectroscopy. Divya and Albert [21] studied the effects of dilution on weld metal microstructure to prevent hot cracking during welding of stainless steel 304B4 using E309 electrode wire filler.

Despite the fact that much previous work has done to investigate the dilution effect on several materials. However, there is still a gap that can be explored, for instance, combination of timing interval wire feeder, the combination of angles, and direction of feeding the filler. With this preliminary investigation, it will get a new perspective on how the inserted method of wire filler in butt joint configuration will affect the macro- and microstructure, in order to understand the effect of intermittent wire feeder on the dilution and segregation effect within various heat input. This paper presents the investigation of the effect of welding parameters on the macrostructure and microstructure of the weld metal and also the mechanical properties of the joint. For this article, the focus will be using one combination proportion of filler metal with various welding parameters.

2 Experimental

The material used in this investigation was AA6063-T5 aluminum alloy plate with a thickness of 3 mm and the type of

Table 2 Mechanical properties of 6063-T5 aluminum alloy

Yield strength (MPa)	Tensile strength (MPa)	Elongation (%)	Hardness (HV)
150–170	190–210	19–21	69–71

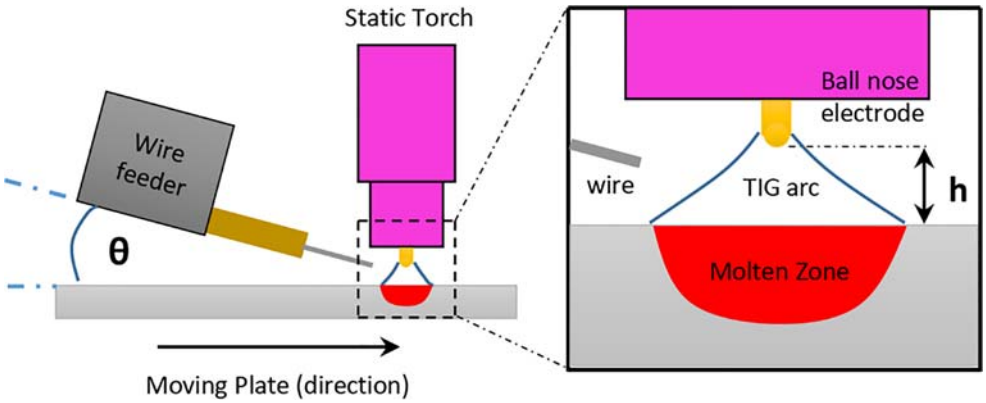

Fig. 1 The TIG welding and wire feeder setup

filler used was ER-5356 wire filler with a diameter of 1.2 mm. A square grove butt joint configuration was made by using two 100 × 50 × 3 mm aluminum plate. The Chemical composition of AA6063-T5 was tested using optical emission spectrometer (OES) using standard ASTM E1251, and the chemical composition of wire filler metal was given in the standard ANSI/AWS A5.10; the nominal chemical composition are listed in Table 1. A tensile test and microhardness measurement were performed to ensure the mechanical strength of the base metal. Results of mechanical properties of base metal AA6063-T5 are listed in Table 2. An illustration of the schematic welding process and the arrangement of the wire feeder, electrode, and moving plate with an automated TIG welding machine is shown in Fig. 1.

High-frequency AC mode was adopted in the TIG welding process with a pulse frequency of 250 Hz and the average excitation voltage during the welding process was between 13 and 14 V. During the welding, high purity argon (99.9%) was applied as the shielding gas with a flow rate of 9 L/min. TIG torch was set perpendicular to the workpiece, and the arc length was set constant at 3 mm. There was no gap in the square butt joint configuration between the two workpieces, and they were clamped using the fixture to avoid distortion. A pure tungsten electrode with a green code AWS class EWTH–2 was employed with a diameter of 2.4 mm. Wire feeder speed

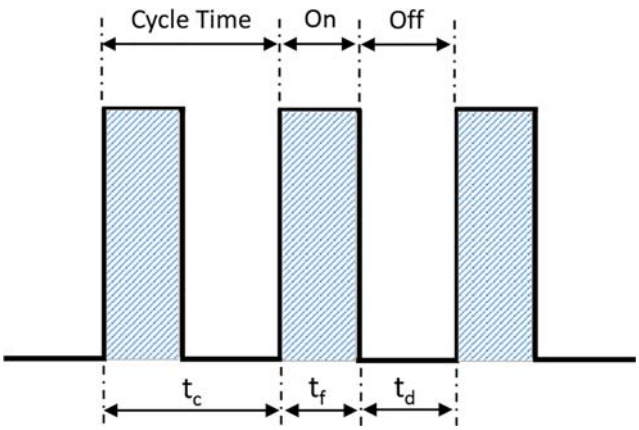

Fig. 2 The wire feeder time control

was set constant at 7.5 mm/s with an intermittent pattern as shown in Fig. 2. The intermittent wire feed has a cycle time of 1.4 s period, with 0.4 s on and 1.0 s off. Wire feeder was set to 15° relative to the workpiece plane. Before the welding process was performed, the workpiece was polished and cleaned with acetone. The selected welding parameters that will be studied are shown in Table 3.

For the macrostructure and microstructure investigation, the specimens followed a standard metallography procedure. The specimens were etched using a 0.5% HF solution. The macrostructure observation was conducted using DINO-LITE, and the microstructure investigation was carried out using Oxion Inverso OX.2153-PLM optical microscope and scanning electron microscope (SEM) with an EDS attached. The tensile test was carried out using 50 kN universal testing machine Tensilon RTF-2350. The specimens were prepared from welded sheets using the CNC milling machine. The specimens' dimension

Table 3 Welding parameters AC–TIG welding process

Process parameter	
Welding current, A	140, 145, 150
Welding speed, mm/min	108, 114, 120
Pre-heating time, s	7
Constant parameter	
Arc voltage, V	13–14
Frequency, Hz	250
Arc length, mm	3
Electrode type	AWS Class: EWTH–2
Electrode diameter, mm	2.4
Shielding gas type	Pure argon (99.95%)
Flow rate, L/min	9
Filler wire type	ER5356
Diameter filler, mm	1.2
Wire feeder speed, mm/s	7.5
Wire feeder angle, θ	15°
Wire feeder method	Intermittent

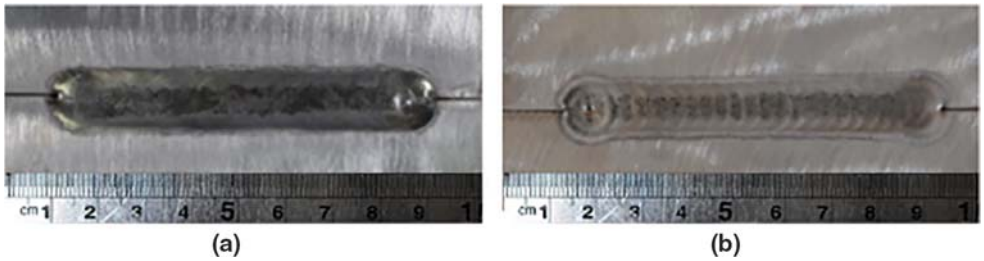

Fig. 3 The weld surface profile of **a** continuous wire filling process and **b** intermittent wire filling process

followed subsize standard of ASTM E-8M. Crosshead displacement rate used was 5 mm/min, and then ultimate tensile strength (UTS) will be plotted with the process parameters. The microhardness of the base metal and the weld metal to HAZ region were measured by using Vickers microhardness machine with a load of 100 g for 15 s hold time, and the distance between every two points was 500 μm. Observation of the fracture surfaces of the tensile tested specimens was performed by an SEM and followed by EDS to observe the chemical composition of the fracture mode.

3 Results

3.1 Macrostructure and weld bead geometry

The weld surface profile of the continuous and the intermittent wire feeder process is shown in Fig. 3. In the continuous wire feeder, the weld beads have higher reinforcement and smooth surface. While in the intermittent wire feeder, the weld beads have a flattened and wavy surface. Higher reinforcement in the continuous wire feeder is caused by more deposited filler into the weld pool compared to the intermittent wire feeder.

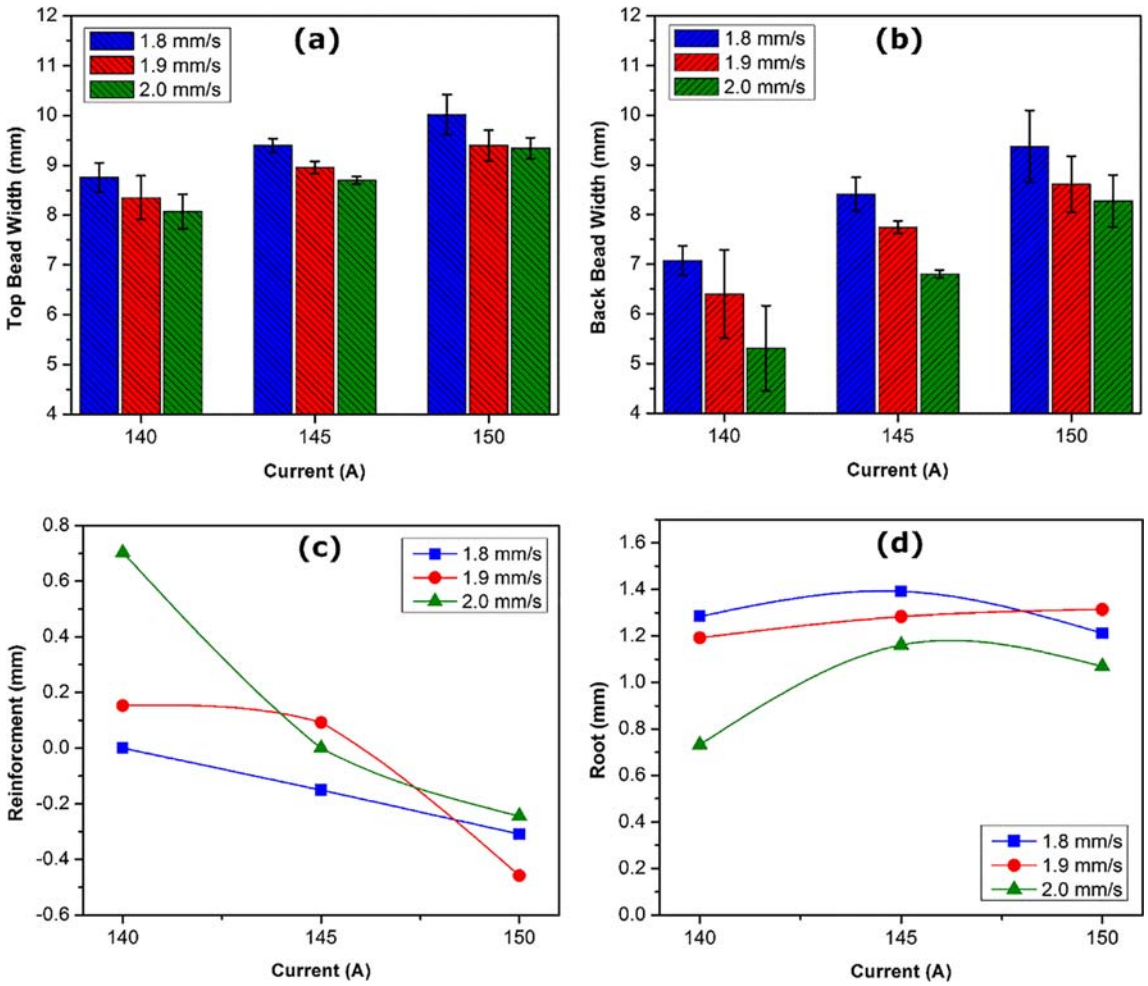

Fig. 4 Geometrical macrostructure on various weld current and welding speed: **a** top bead width (TBW), **b** back bead width (BBW), **c** reinforcement, and **d** root

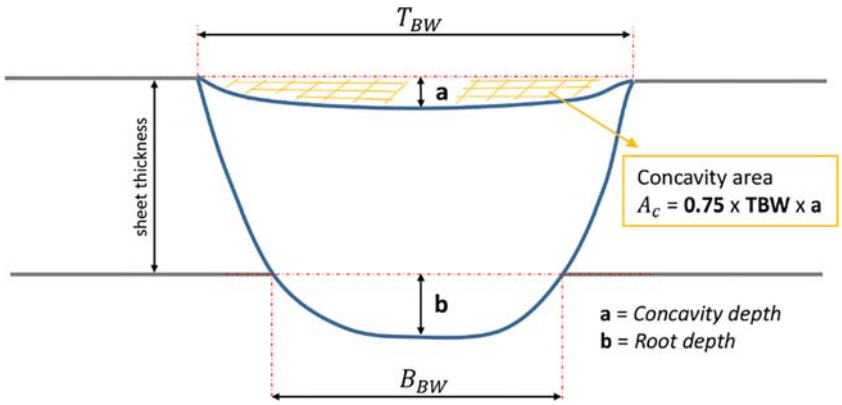

Fig. 5 The cross-sectional weld metal area

Figure 4a, b shows an increase in top bead width (TBW) and back bead width (BBW) when weld current increased and welding speed decreased. Figure 4c shows reduced the height of reinforcement when weld current increased, and it showed that the concave profile occurred in 150 A welding current. Figure 4d shows slightly increased in root depth when weld current increased, or welding speed decreased. The welding process was done in the same parameter condition and using the same deposit filler rate. An increase in weld current or decrease in welding speed had a result in the increase of heat input per weld length (J/mm), consequently increasing the TBW and BBW, decreasing the height of reinforcement, and increasing the depth of root. Therefore, under the condition of good weld acceptability, the rate of deposit filler can also be increased when the heat input is increased.

The ratio of filler regarding the length and volume is calculated using Eqs. (1) and (2). R_L is the length ratio between the total length of filler in one cycle time (L) over the distance traveled by the torch in one cycle time (D). Variables v_f, v_w, t_f, t_d, and t_c respectively are wire feeder speed, welding speed, feeder time, delay time, and cycle time.

$$R_L = \frac{L}{D} = \frac{v_f.\ t_f}{v_w.\ t_c} \tag{1}$$

R_V is the volume ratio between the total volume of filler in one cycle time (V_L) over the volume of the welded zone in one cycle time (V_D), where A_f and A_{wz} respectively are the cross-sectional area of the filler (circular area) and the cross-sectional area of the welded zone (trapezoidal area).

$$R_V = \frac{V_L}{V_D} = \frac{L.\ A_f}{D.\ A_{wz}} = R_L \frac{A_f}{A_{wz}} \tag{2}$$

A_{wz} can be calculated using trapezoid (Eq. (3)) with T_{BW} and B_{BW} as top bead width and bottom bead width respectively (Fig. 5),

$$A_{wz} = \left(\frac{T_{BW} + B_{BW}}{2}\right) \times \text{sheet thickness} \tag{3}$$

The wire feeder speed (v_f) was set constant at 7.5 mm/s and using the delay time (t_d) 1 s and feeder time (t_f) 0.4 s, the length ratio (R_L) and the volume ratio are given in Table 4.

Figure 6 shows the pictures of the cross-section of the weld metal (WM) in different welding parameters. With the lower heat input per length (J/mm) and higher volume ratio, the reinforcement at top weld bead occurred at 140 A welding current and 2 mm/s welding speed. However, the low heat input large pores take place on the WM, resulting in a weak joint and the failure modes might have located in WM. With more heat input, the reinforcement is reduced and large pores dissolved to smaller pores (micropores). While using weld current 150 A, a volume of deposit filler compared to molten metal is too small, so that the deposited filler is not enough to cover the attraction of liquid metal down due to gravity. Hence, weld bead's concavity occurs. The concavity is formed because of displacement or metal ejection from the weld pool during welding process [22]. The concavity is the result of higher heat input per length. The higher heat input was obtained from the higher current and lower welding speed. Higher heat input causes more base metals to melt and has a higher liquid temperature. The increase in liquid metal temperature causes the surface tension to decrease and the time to solidify becomes longer; consequently, the molten metal is attracted by gravity with a longer duration. Hence, concavity inevitably

Table 4 Calculated of length ratio (R_L) and volume ratio (R_V) in different welding speed and welding current

Welding speed	R_L	R_V (10^{-2})		
1.8 mm/s	1.19	5.67 ± 0.21	5.04 ± 0.14	4.63 ± 0.27
1.9 mm/s	1.13	5.76 ± 0.52	5.09 ± 0.10	4.72 ± 0.23
2.0 mm/s	1.07	6.04 ± 0.55	5.21 ± 0.13	4.59 ± 0.19
	All current	140 A	145 A	150 A

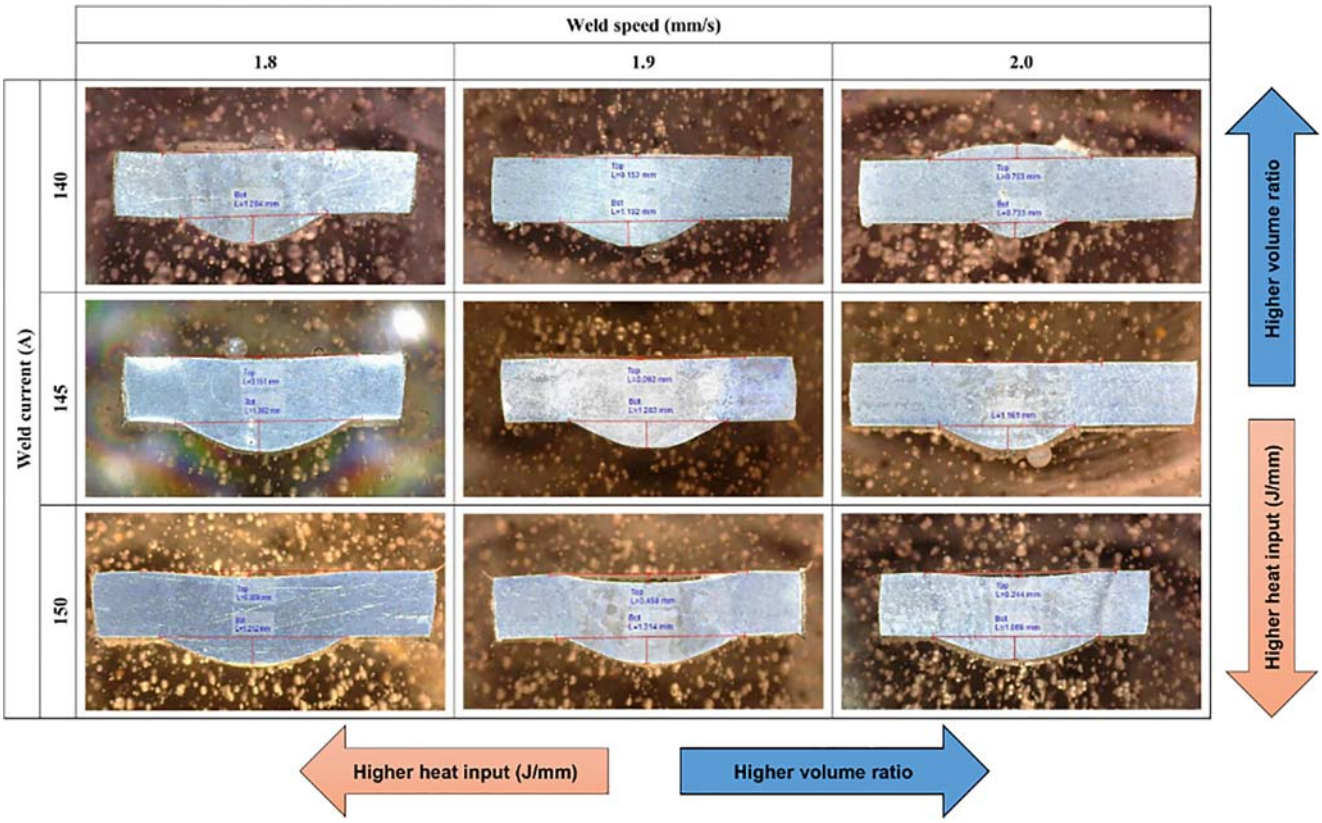

Fig. 6 Cross-section of the weld metal in different welding parameters

occurred. As shown in Table 4, the volume ratio (R_V) of 0.0521 (145 A–2.0 mm/s) is the minimum value so that concavity of weld bead does not occur; therefore, acceptable $R_V \geq 0.06$ is where weld current is in the range of 140–150 A.

In order to increase the volume ratio (R_V) using weld current 150 A, the volume of concavity needs to be calculated using the Eq. (4), where A_C is the concavity area that can be seen in Fig. 5 and D is the distance traveled by the torch in one cycle time, which is the same as Eq. (1).

$$V_{CON} = A_C \times D \tag{4}$$

Using the sample 150–2 mm/s, the depth of concavity is approximately $a = 0.244$ mm, $T_{BW} = 9.3 \pm 0.2$ mm, and $D = 2.8$ mm. So the filler needed to be added is approximately the same as the $V_{CON} = 4.765$ mm^3. Because the area of filler is $A_f = 1.131$ mm^2, therefore, the length of filler to be added is approximately 4.2 mm, and because the initial length of filler is 3 mm, hence, the total filler to be added is approximately 7.2 mm. If v_f, v_w, and t_c have the same value, therefore, $t_f =$

Table 5 New calculated of length ratio (R_L) and volume ratio (R_V) depend on the depth of concavity

	140 A		145 A		150 A	
	R_L	R_V	R_L	R_V	R_L	R_V
1.8	–	–	2.01	0.0852	3.12	0.1215
1.9	–	–	1.62	0.0730	3.92	0.1644
2.0	–	–	1.07	0.0521	2.58	0.1106

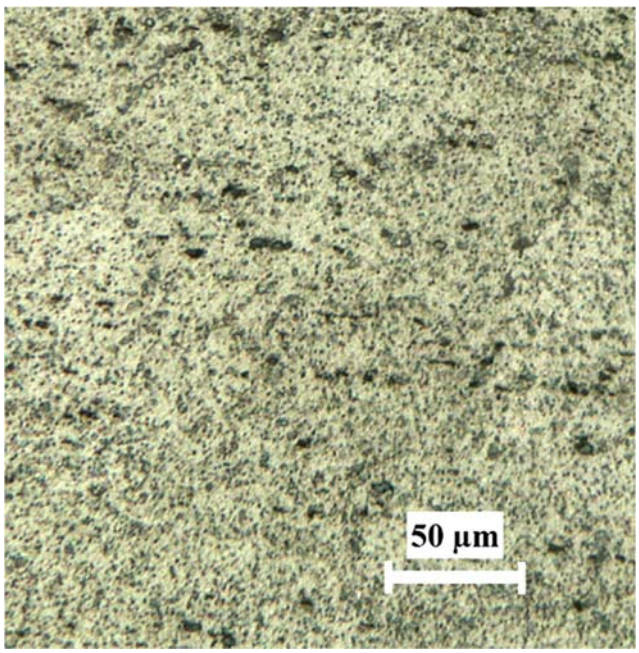

Fig. 7 Microstructure of base metal AA6063

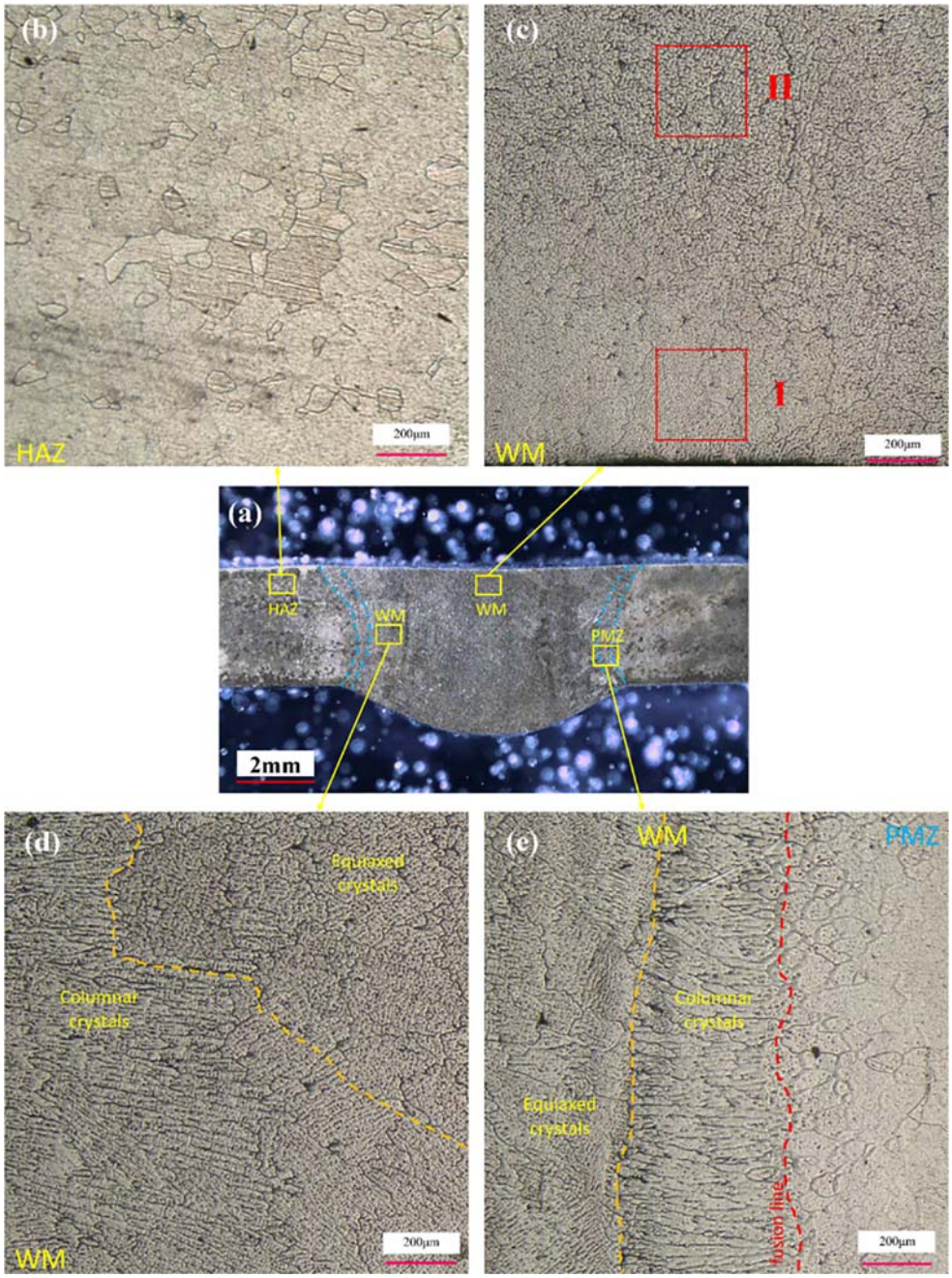

Fig. 8 Microstructure in different areas of the joints (weld current = 145 A, welding speed = 1.9 mm/s). **a** Macroscopic area. **b** Heat-affected zone (HAZ). **c** Weld metal (WM) at near top surface. **d** Weld metal (WM) at near fusion line. **e** Partial melted zone (PMZ) and fusion line

0.96 s and $t_d = 0.44$ s, respectively. New ratio of length and volume are $R_L = 2.57$ and $R_V = 0.11$. All the parameters that result in concavity can be calculated using the same method. The calculation results are shown in Table 5.

However, the value in Table 5 is just an approximation of how much deposit filler needs to be added based on the preliminary investigation of the geometrical cross-section of the weld metal. In actual condition, when filler rate deposit increases, demands of heat input are increased too. In the case of same heat input applied while filler rate increased, partially more heat needs to be used to melt the filler, and consequently less heat is used to melt the base metal. Less molten base metal and more filler will produce a higher volume ratio compared to the calculated value. Therefore, using this calculated ratio, the tendency of weld beads to have reinforcement at TBW is high. There is a need to be considered when heat input is not enough because precipitation of large pores could occur.

3.2 Microstructure

Microscopic observations in different areas of the joints are displayed in Fig. 7 and Fig. 8. The sample parameters are weld current 145 A and welding speed 1.9 mm/s with

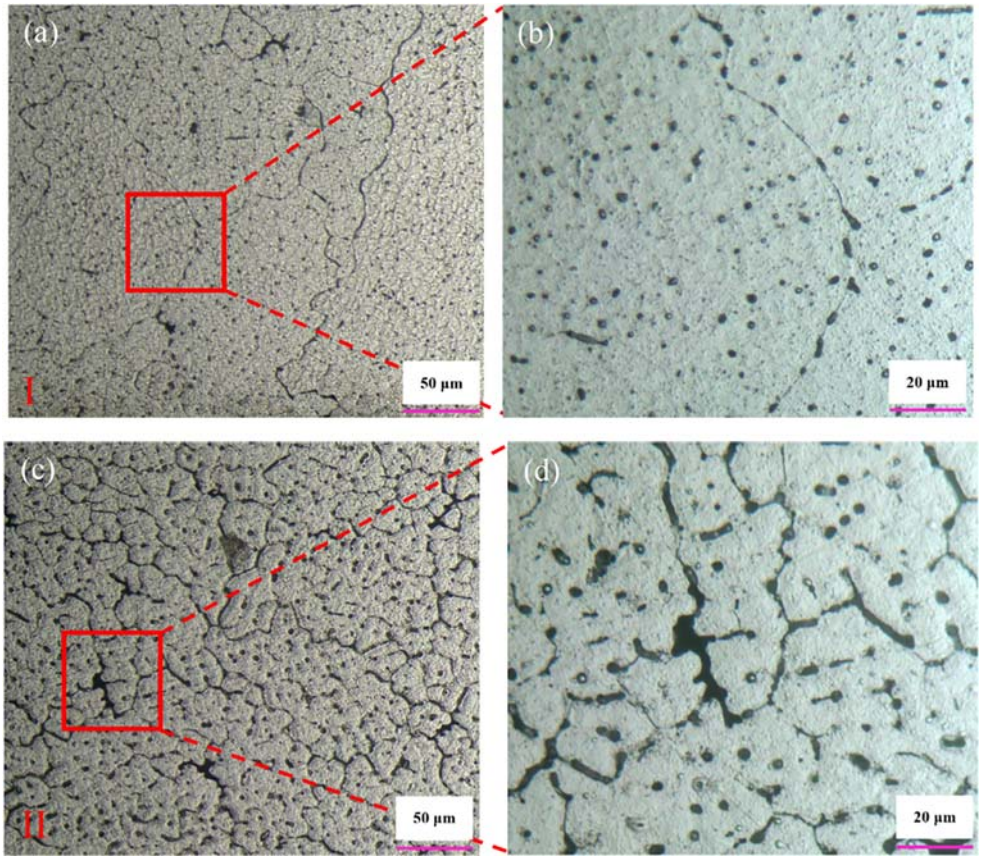

Fig. 9 **a**–**d** Magnification 200× and 500× from Fig. 8c

a medium level of heat input. As shown in Fig. 8a, the typical microstructures can be divided into four visible zones which are weld metal (WM), partially melted zone (PMZ), heat-affected zone (HAZ), and base metal (BM) [23].

BM As shown in Fig. 7, observation on the base metal area indicated that the primary α-Al (aluminum solid solution) which is marked by light color and the second phase of Mg–Si eutectic phase and Al–Mg eutectic phase which are marked by dark color. Both eutectic phases present in homogeneous

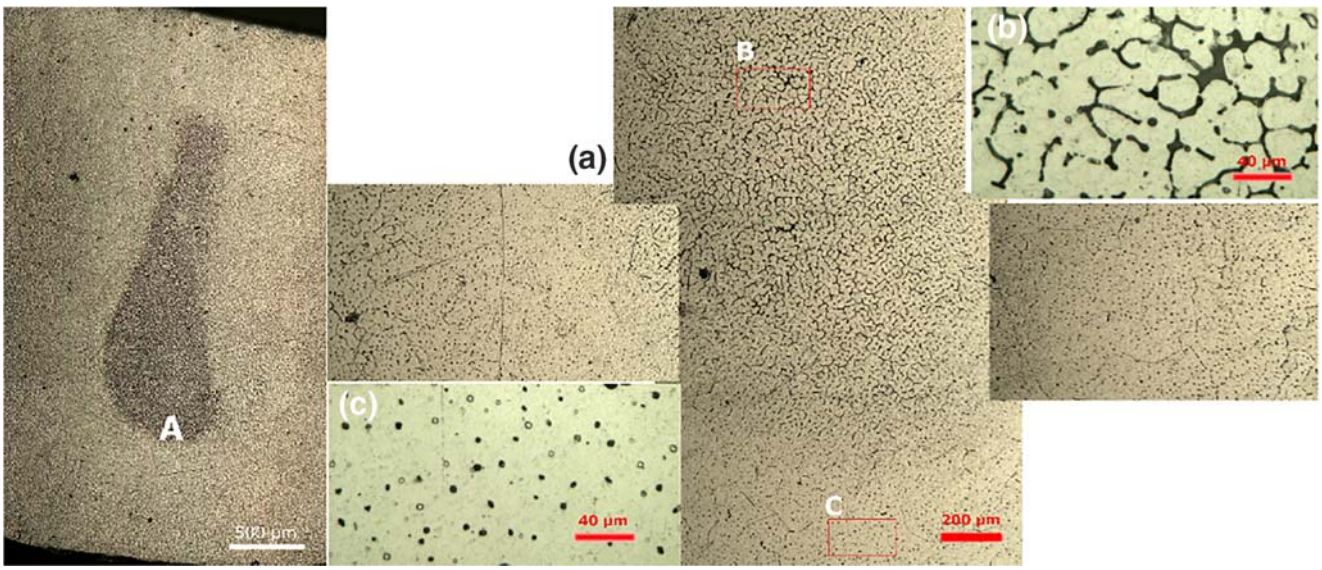

Fig. 10 Wire dilution with sample parameter of weld current 150 A and welding speed 2.0 mm/s. (a) The phenomenon of segregation occurs at the WM center area, (b) dense eutectic phase on localized segregation, and (c) globular shaped eutectic phase outside the localized segregation area

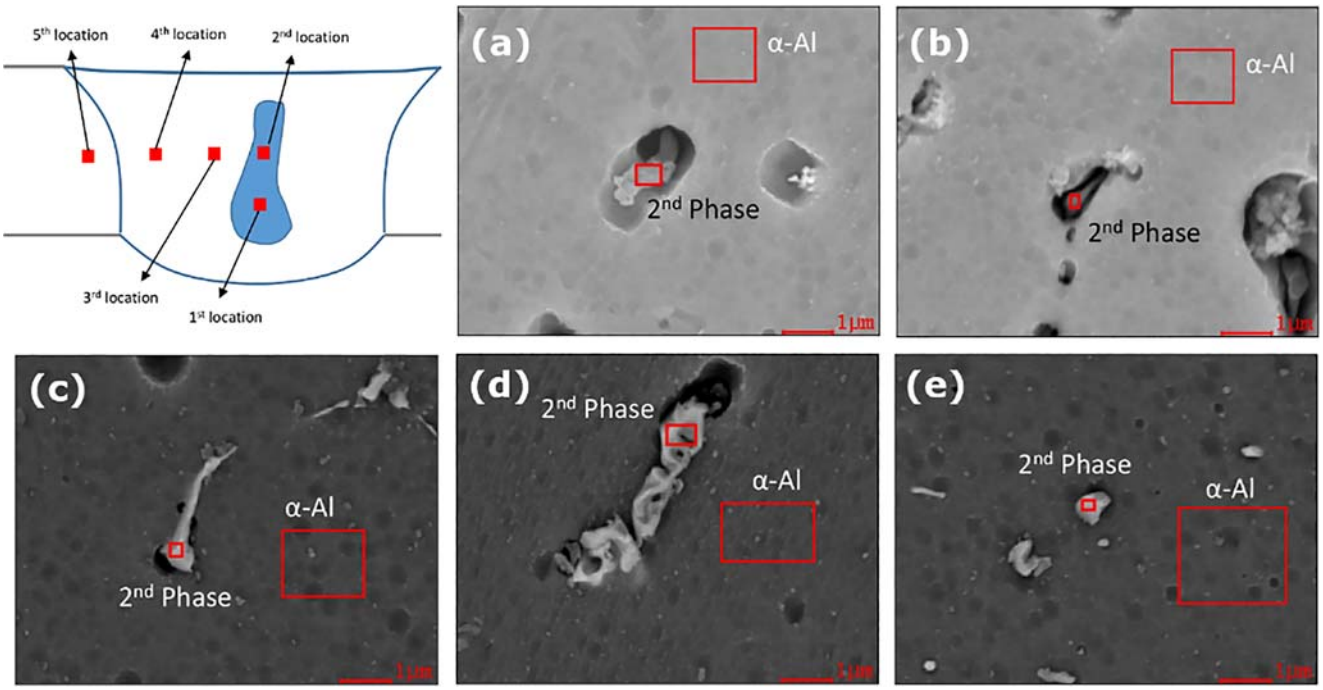

Fig. 11 EDS study on α-Al matrix and the second phase particle

distribution intra-grain formed globular small shape within less than 10 μm to nm scale.

HAZ This area was subjected to a longer temperature of above 200 °C or ranging from 150 to 300 °C during the welding process and cooling process, so it takes a longer time to grow up the grain. Hence, the grain becomes coarser and larger compared to that in PMZ [23]. The grains grew up and formed new equiaxed grains with non-homogeneous size (Fig. 8b). The HAZ region is similar to the results shown by [6], although they used pulsed TIG welding. It is shown that the welding thermal cycle affects the eutectic phase to be dissolved in the aluminum matrix. Increasing grain size may also reduce the mechanical properties of Al–Mg–Si alloys such as hardness, tensile strength, and toughness.

Table 6 EDS analysis (wt%) in five location of second phase particle and α-Al matrix

No.	Second phase				α-Al matrix			
	Al	Mg	Si	Fe	Al	Mg	Si	Fe
1	79.77	2.22	18.01	–	97.54	2.26	0.18	–
2	87.89	3.09	9.02	–	97.11	2.54	0.33	–
3	87.11	1.86	6.94	4.09	98.57	1.37	0.19	–
4	90.81	1.46	4.70	3.03	98.04	1.96	–	–
5	94.53	1.01	2.79	1.66	96.17	1.17	1.93	0.73

PMZ In Fig. 8e near the fusion line (as shown in red line), the PMZ region shows the growth of new equiaxed grains forming a smaller size compared to the grain size in the HAZ area. In this area where the temperature reached more than 350 up to 450 °C, some of the Mg_2Al_3 will be redissolved and closer to the weld where the temperatures reach to 560 °C, partial melting occurs causing some shrinkage cavitation and formed fusion line.

WM The weld area is composed of dendritic structure mostly found at the center area (Fig. 8c) and columnar structure found at near fusion line (Fig. 8d, e). The columnar structure width area is approximately 0.5–1 mm, which grew from fusion line toward the center of the weld. In the center of WM, the crystals shape are mostly in equiaxed form and are approximately 10–20 μm in diameter (Fig. 9c). However, in some area, a larger equiaxed structure can be found with very thin precipitation in the boundary layer and presents a homogeneous distribution of globular shaped precipitation intra-grain (Fig. 9a). Figure 10(a) shows the results of wire dilution with parameter weld current 150 A and welding speed 2.0 mm/s, and the phenomenon of segregation occurs at the center area where the wire was inserted. The localized segregation of Al–Mg_2Si eutectic structure could be attributed to the high concentration of magnesium from the additive wire ER5356. Figure 10(b) shows the dense eutectic phase on the body of localized segregation and Fig. 10(c) shows globular shaped eutectic phase with a small size spread evenly and sparse, and the location is outside and near the localized region.

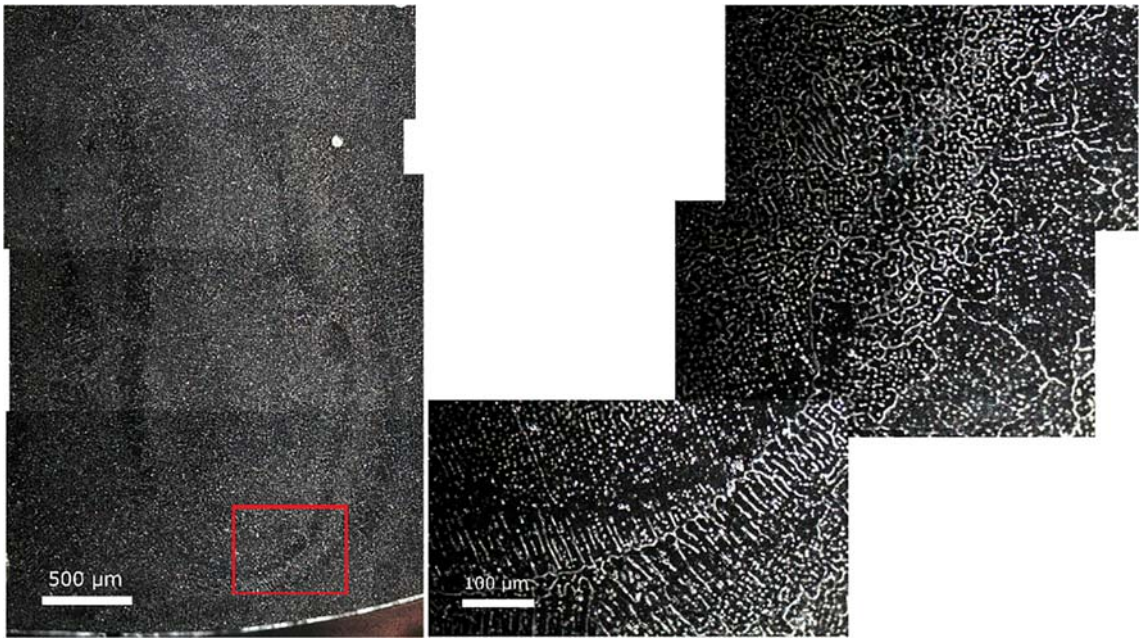

Fig. 12 Wire dilution with sample parameter of weld current 150 A and welding speed 1.8 mm/s

Figure 11 shows the EDS study of the Mg and Si solute content on the α-Al matrix and the second phase particle. Si was the major alloy element on the second phase particle in the localized segregation (numbers 1 and 2). Very high Si content in location number 1 makes the Al–Si eutectic structure dominant compared to Mg_2Si, while in location number 2, higher content of Mg and lower content of Si compared to number 1 make Mg_2Si more rich and with less Al–Si eutectic phase. Al–Si–Mg–Fe structure is found at location numbers 3, 4, and 5; in contrast, there is no Fe content on location numbers 1 and 2. Location 3 near the localized segregation is where the globular eutectic structure was found mostly in this region, location 4 is in the columnar structure near the weld lines, and location 5 was located at the HAZ region. Si, Mg, and Fe contents on the locations 3, 4, and 5 reduce gradually and have lower value in the location at the HAZ region

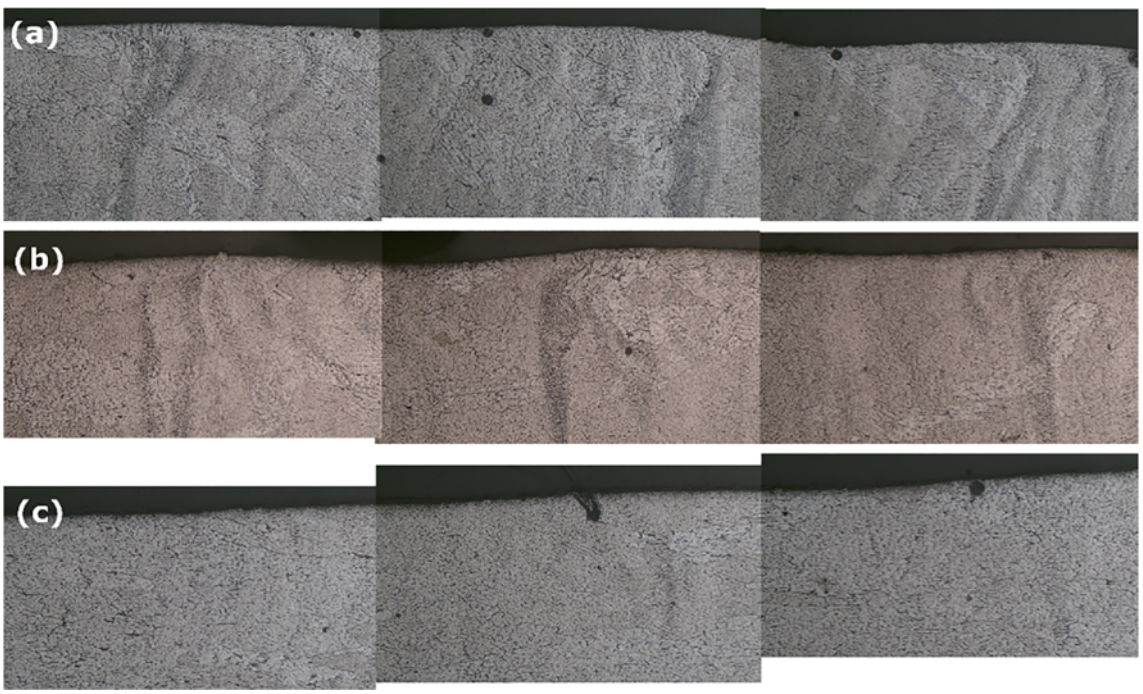

Fig. 13 Traverse section of the specimen: **a** weld current 140 A and welding speed 2 mm/s, **b** weld current 145 A and welding speed 1.9 mm/s, and **c** weld current 150 A and welding speed 1.8 mm/s

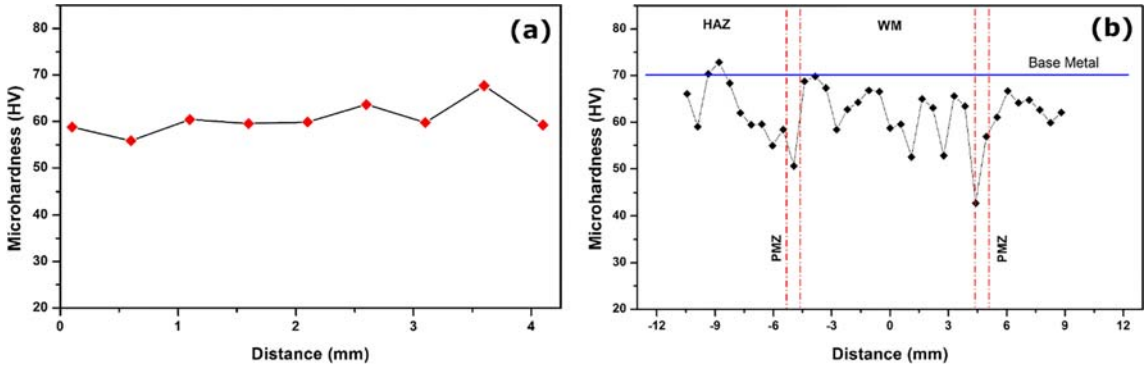

Fig. 14 **a** Microhardness of WM in vertical distribution across the center of WM from top bead to back bead. **b** Microhardness of horizontal distribution across HAZ, PMZ, and WM

(number 5). In the localized segregation, Mg element has high solute content both in the second phase and aluminum matrix (Mg > 2%) compared to the outside region (Mg < 2%). As shown in Table 6, Si element on the α-Al matrix was minimal. Si elements tend to react with Al and form segregation of Al–Si eutectic structure and cause losses of Si element in matrix composition. Hence, the weld metal region contained low Si with more Mg solute content at the α-Al matrix composition. In the HAZ region, Si content was higher (1.93%) because there is no melting phase which causes Al and Si being bound together; hence, Si element was a persistence solute on the α-Al matrix.

Figure 12 shows the sample with parameters weld current 150 A and welding speed 1.8 mm/s. As shown in Fig. 12 the columnar structure in dilution boundaries shows the occurrence of fast cooling rates while the wire was inserted and resulted in the localization of segregation. Wang et al. [24] found that the direction of grain growth and the orientation of grain structure might be attributed to the directional cooling when the wire was inserted and the highest temperature gradient are located in the boundary of melted metal and the wire filler. This is similar to the columnar crystal contained in WM near the weld lines. Figure 13a–c shows the traverse section of the specimen of 140-2 (weld current 140 A and welding speed 2 mm/s), 145-1.9 (weld current 145 A and welding speed 1.9 mm/s), and 150-1.8 (weld current 150 A and welding speed 1.8 mm/s) respectively. The specimen 140-2 was the lowest heat input, 145-1.9 was the medium heat input, and 150–1.8 was the highest heat input in all 9 specimens. Figure 13a shows the wavy-like structure that was caused by fast solidification rate of wire filler. In Fig. 13b, wavy-like structure was reduced to some degree and disappeared in Fig. 13c. The wavy-like structure depended on how much heat would be added. The more heat was added, the longer the melting time; hence, the solidification rate would be reduced and therefore the wavy-like structure could be minimized.

3.3 Mechanical properties and failure mechanics

Microhardness distribution is recorded by performing Vickers indentations on the TIG metallographic sample. A force of 100 gf with 15 s dwell time is used, and a spacing between

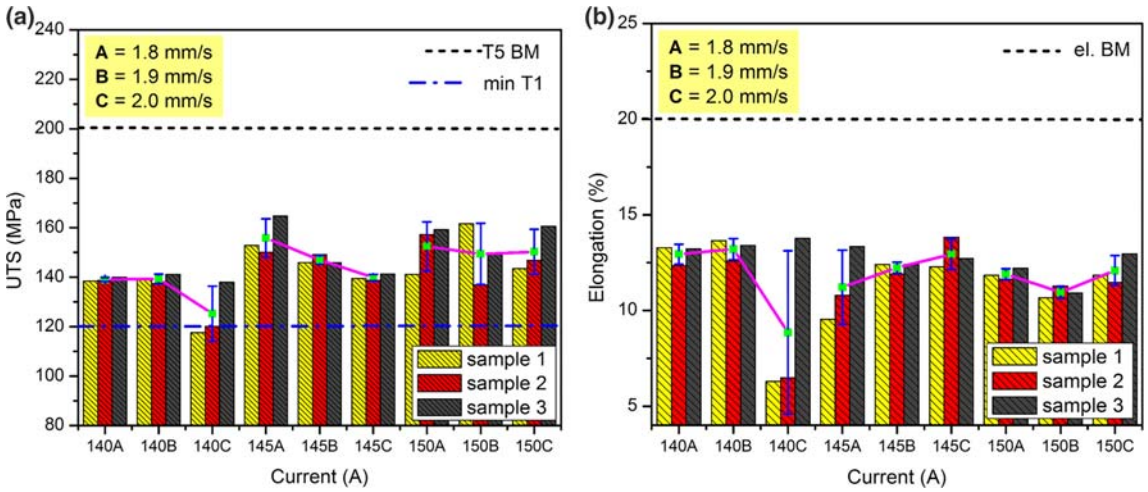

Fig. 15 **a** Ultimate tensile strength (UTS) and **b** elongation are plotted in different welding current and welding speed in comparison to a base metal (BM) of AA6063-T5

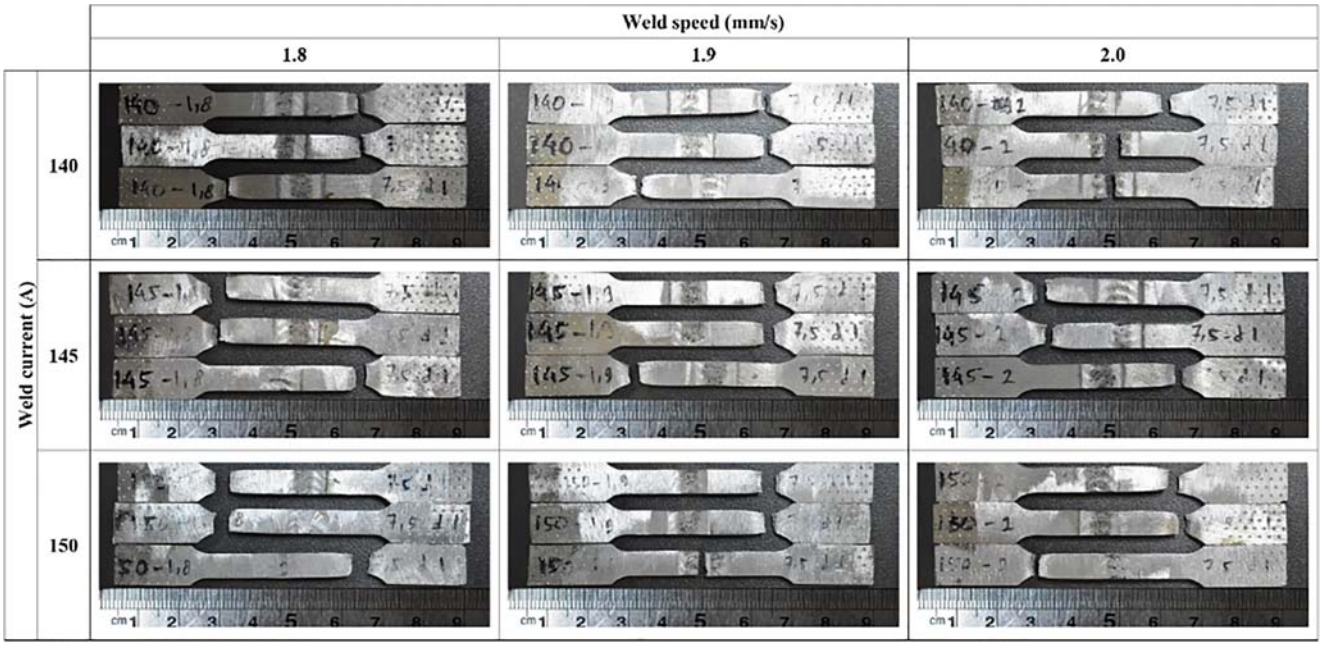

Fig. 16 Fracture location of all specimens

indentations is 500 μm. Indentations are made on the horizontal distribution across the HAZ, PMZ, and WM, and the vertical distribution across the top of WM to the bottom of WM. Microhardness profile distribution is carried out on the horizontal distribution with approximately 10 mm to the right and to the left from the center of the weld. Figure 14a shows microhardness of WM in vertical distribution across the center of WM from top bead to back bead, and the average value is 60.4 ± 3.4 HV. There are nine locations of indentation which is divided into two distinct regions, the upper zone and the lower zone. The upper zone consists of the first four locations of hardness between the distance 0–2 mm and lower zone consists of the last four locations of hardness between the distance 2–4 mm. The average value of hardness at the lower zone is 62.4 ± 4.2 HV and the upper zone is 58.5 ± 2.0 HV. This graph shows that the hardness in the lower zone has a slight increase compared to the upper zone. Figure 14b shows microhardness of horizontal distribution across HAZ, PMZ, and WM. This graph shows a microhardness value of weld metal (WM) with an average value of 62.8 ± 5.2 HV, the maximum value is 69.8 HV and the minimum is 52.5 HV. The lowest value of microhardness is in the PMZ area, near the fusion line. The lowest value on the right side is 43 HV, while on the left side is 51 HV. After that, the hardness value gradually increases to near the value of BM. Chen et al. [25] reported that the hardness value would decrease with an increase in temperature within 287–414 °C. The lowest hardness was obtained at 452 °C peak temperature during welding process within 1 day of natural aging (NA) treatment, and after 1-month NA treatment, the lowest hardness can be achieved approximately within a range temperature of 420–470 °C. And then the hardness will increase gradually until the temperature reached 504 °C, then the hardness approaches stable horizontal distribution.

As shown in Fig. 15, the ultimate tensile strength (UTS) and elongation are plotted in different welding current and welding speed in comparison to a base metal (BM) of AA6063-T5 and minimum UTS of AA6063-T1. Each sample named with a number and an alphabet: 140A, in which 140 is welding current and A means welding speed 1.8 mm/s. Every combination parameters take 3 samples each. In total, there are 27 samples taken into tensile testing. Most of the specimens

Table 8 Average ultimate tensile strength (MPa) and elongation (%)

Welding speed	Weld current					
	140 A		145 A		150 A	
	UTS	El.	UTS	El.	UTS	El.
1.8 mm/s	139.0 ± 0.8	12.9 ± 0.5	155.8 ± 7.8	11.2 ± 1.9	152.5 ± 9.9	11.9 ± 0.3
1.9 mm/s	139.3 ± 1.9	13.2 ± 0.6	147.0 ± 1.8	12.2 ± 0.3	149.4 ± 12.4	10.9 ± 0.3
2.0 mm/s	125.3 ± 11.1	8.8 ± 4.3	139.9 ± 1.3	12.9 ± 0.8	150.3 ± 9.1	12.1 ± 0.8

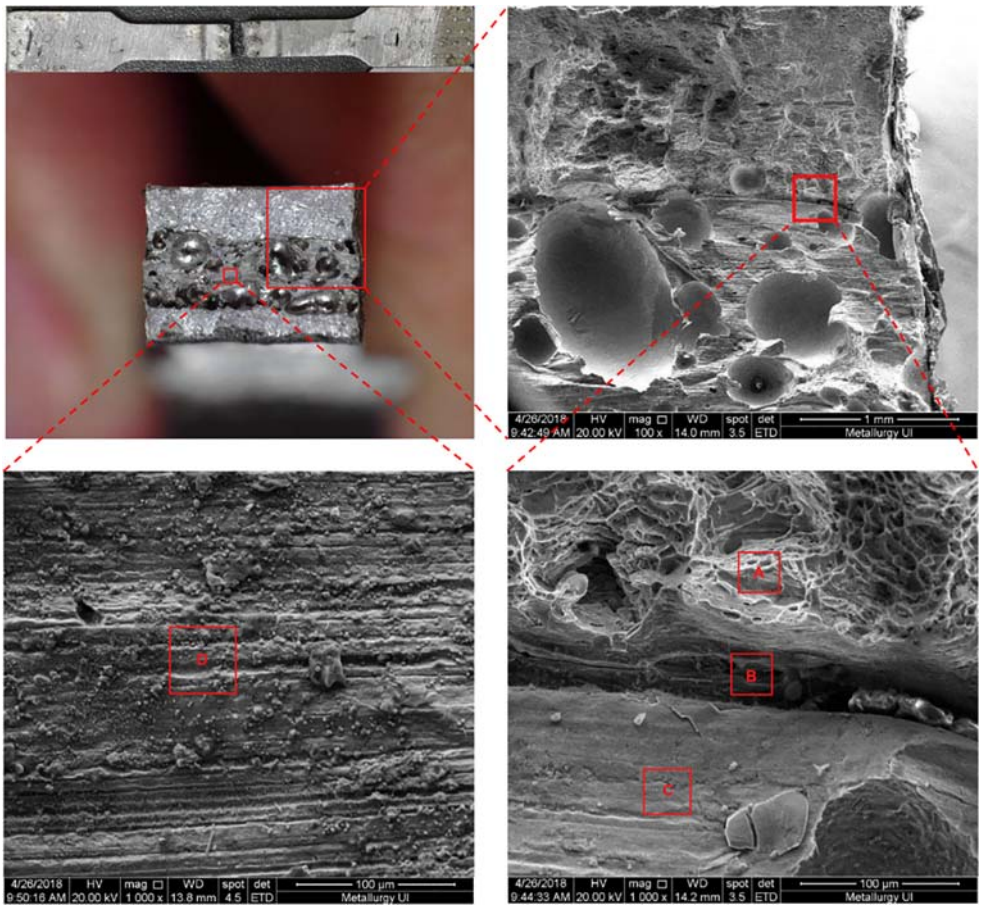

Fig. 17 Fracture mode samples that undergo oxidation

would fracture at the HAZ area (Fig. 16) between 1 and 1.5 mm from the center of the weld and has UTS at least 140 MPa, elongation between 10 and 13% (Table 8). It shows that the strength is reduced between 20 and 30%. Figure 16 shows that sample 140C has 2 out of 3 samples that failed at WM and tensile test result indicates that UTS and elongation are no more than 120 MPa and 7%, respectively. This result shows that lack of heat input has a high potential to fracture at WM and also less heat input has a tendency to have lower UTS at some level. Figure 17 shows that the primary cause of weld metal fracture is oxidation at the low melting temperature. At low melting temperature, the molten metal produces excessive turbulence that allows the oxygen to be trapped into the molten metal; therefore, large porosity occurs. Table 7 shows the EDS analysis of four locations A through D in Fig. 17. Locations A, B, and C are located in the boundaries between the oxidation region and free of oxidation. Location A in Fig. 17 shows the fractographs showing the ductile manner where dimples and large void occurred. Location B which was shaped like a cliff indicates the boundary between oxidized and not. Locations C and D show the brittle fracture manner; in location C, the cleavage step was visible and in location D, tearing ridge was visible. Figure 18 shows the typical fracture location of the specimen that breaks at the HAZ region. The fracture surface in the welded samples shows normal ductile behavior. In that case, a ductile fracture with a mixture of many microvoids and coarse dimples is obtained (Table 8).

Table 7 EDS analysis (wt%) of WM fracture caused by oxidation

Loc.	Elements			
	Al	Mg	Si	O
A	97.57	2.43	–	–
B	82.41	2.79	2.46	12.34
C	81.21	3.68	2.93	12.18
D	60.41	4.78	2.39	32.42

4 Conclusions

Based on macrostructure, microstructure, SEM-EDS, and mechanical property results, it can be concluded that effect of wire feeding technique on the dilution on AA6063-T5 with ER5356 filler metal using tungsten inert gas (TIG) welding can be summarized as follows:

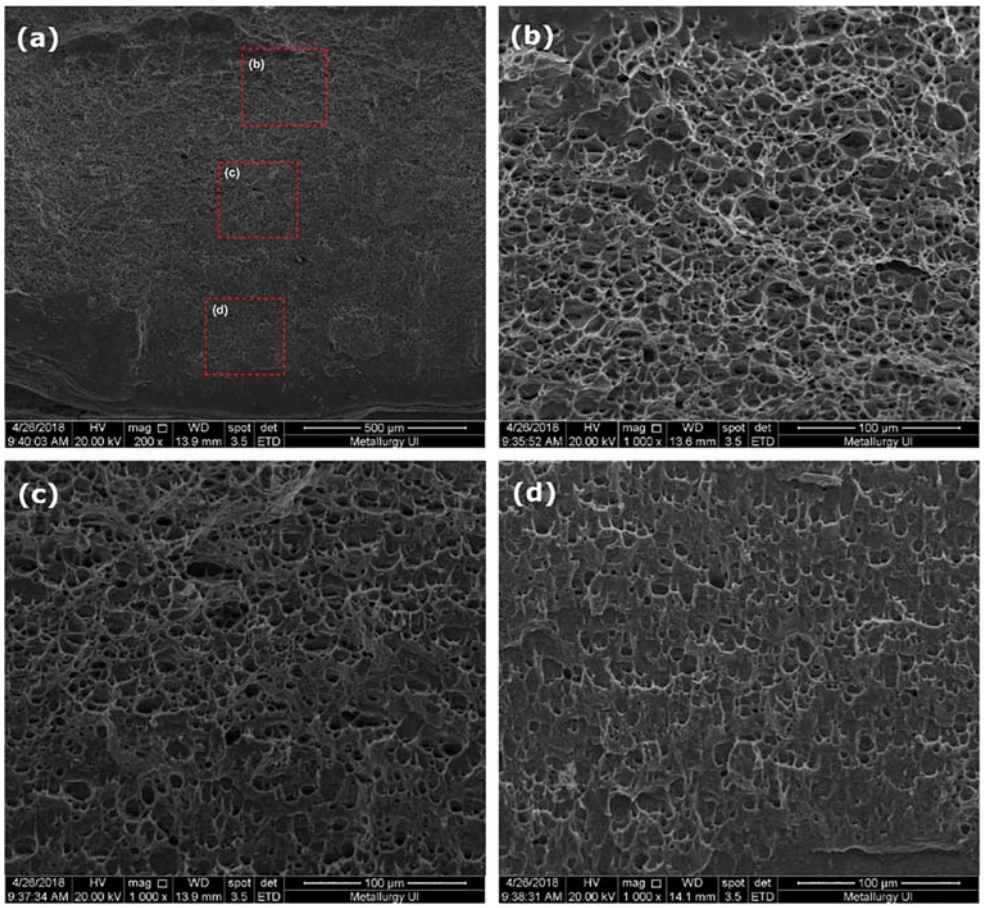

Fig. 18 **a**–**d** Fracture mode at the HAZ area

1. Between continuous and intermittent wire feeder, the top surface weld beads have different contours. While increasing weld current and/or decreasing welding speed, the top bead width (TBW) and back bead width (BBW) increase in size and also change the reinforcement significantly from convexity profile to concavity profile.
2. The proposed method of length ratio (R_L) and the volume ratio (R_V) could estimate the minimum value of ratio under the condition of a good welded surface profile. The acceptability of volume ratio in order for concavity of weld bead not to occur is $R_V \geq 0.06$, where weld current is in the range of 140–150 A. Therefore, under the condition of good weld acceptability, the rate of deposit filler can also be increased when the heat input is increased.
3. The microstructure showed that the wire dilution and the phenomenon of localized segregation occurred at the center area. EDS study reveals that Mg and Si elements on the α-Al matrix and the eutectic phase particle are the major alloy element on the localized segregation. Magnesium content was found higher at localized segregation compared to the outside localized segregation.
4. The microstructure shows that columnar structure was formed in dilution boundaries, and it reveals that fast cooling rates happened when the filler wire was inserted. Also, microstructure on weld traverse section shows that the wavy-like structure depended on the heat input.
5. Ultimate tensile strength shows that specimens that lack heat input were susceptible to oxidation at WM. In the fracture mode showing samples that undergo oxidation, the fracture will occur at weld metal at the brittle manner and reduce the strength up to 40%; otherwise, if the heat input is fulfilled, the fracture tends to occur at the HAZ area with ductile behavior and reduces the strength by 25–30%.

Acknowledgments The authors would like to express their sincere gratitude for the financial support from PDUPT RISTEK DIKTI 2018 with contract number 397/UN2.R3.1/HKP 05.00/2018.

References

1. Manti R, Dwivedi DK, Agarwal A (2008) Microstructure and hardness of Al-Mg-Si weldments produced by pulse GTA welding. Int J Adv Manuf Technol 36(3–4):263–269
2. Imam M, Racherla V, Biswas K (2014) Effect of post-weld natural aging on mechanical and microstructural properties of friction stir welded 6063-T4 aluminum alloy. Mater Des 64:675–686
3. Ahmad R, Bakar MA (2011) Effect of a post-weld heat treatment on the mechanical and microstructure properties of AA6061 joints

welded by the gas metal arc welding cold metal transfer method. Mater Des 32(10):5120–5126
4. Lakshminarayanan AK, Balasubramanian V, Elangovan K (2009) Effect of welding processes on tensile properties of AA6061 aluminum alloy joints. Int J Adv Manuf Technol 40(3):286–296
5. Manti R, Dwivedi DK, Agarwal A (2008) Pulse TIG welding of two Al-Mg-Si alloys. J Mater Eng Perform 17(5):667–673
6. Manti R, Dwivedi DK (2007) Microstructure of Al-Mg-Si weld joints produced by pulse TIG welding. Mater Manuf Process 22(1):57–61
7. Mathers G (2002) The welding of aluminum and its alloys. Woodhead Publishing Ltd, Cambridge
8. Wu YE, Wang YT (2010) Enhanced SCC resistance of AA7005 welds with appropriate filler metal and post-welding heat treatment. Theor Appl Fract Mech 54(1):19–26
9. Devendranath Ramkumar K, Chandrasekhar A, Srivastava A, Preyas H, Chandra S, Dev S, Arivazhagan N (2016) Effects of filler metals on the segregation, mechanical properties and hot corrosion behavior of pulsed current gas tungsten arc welded super-austenitic stainless steel. J Manuf Process 24:46–61
10. Shen X, Ma G, Chen P (2018) Effect of welding process parameters on hybrid GMAW-GTAW welding process of AZ31B magnesium alloy. Int J Adv Manuf Technol 94(5–8):2811–2819
11. Liang Y, Hu S, Shen J, Zhang H, Wang P (2017) Geometrical and microstructural characteristics of the TIG-CMT hybrid welding in 6061 aluminum alloy cladding. J Mater Process Technol 239:18–30
12. Ning J, Zhang LJ, Na SJ, Yin XQ, Niu J, Zhang JX, Wang HR (2017) Numerical study of the effect of laser-arc distance on laser energy coupling in pulsed Nd: YAG laser/TIG hybrid welding. Int J Adv Manuf Technol 91(1–4):1129–1143
13. He Y, Tang X, Zhu C, Lu F, Cui H (2017) Study on insufficient fusion of NG-GMAW for 5083 Al alloy. Int J Adv Manuf Technol 92(9–12):4303–4313
14. Zhu C, Tang X, He Y, Lu F, Cui H (2017) Study on arc characteristics and their influences on weld bead geometry in narrow gap GMAW of 5083 Al-alloy. Int J Adv Manuf Technol 90(9–12): 2513–2525
15. Zhang Y, Huang J, Cheng Z, Ye Z, Chi H, Peng L, Chen S (2016) Study on MIG-TIG double-sided arc welding-brazing of aluminum and stainless steel. Mater Lett 172:146–148
16. Banovic SW, DuPont JN, Marder AR (2001) Dilution control in gas-tungsten-arc welds involving superaustenitic stainless steels and nickel-based alloys. Metall Mater Trans B Process Metall Mater Process Sci 32(6):1171–1176
17. Banovic SW, DuPont JN, Marder AR (2002) Dilution and microsegregation in dissimilar metal welds between super austenitic stainless steel and nickel base alloys. Sci Technol Weld Join 7(6):374–383
18. Ahn Y, Yoon B, Kim H, Lee C (2002) Effect of dilution on the behavior of solidification cracking in PTAW overlay deposit on Ni-base superalloys. Met Mater Int 8(5):469–477
19. Pickin CG, Williams SW, Lunt M (2011) Characterisation of the cold metal transfer (CMT) process and its application for low dilution cladding. J Mater Process Technol 211(3):496–502
20. Miná EM, da Silva YC, Dille J, Carvalho Silva C (2017) Effect of dilution on the microstructure of AWS ERNiCrMo-14 alloy in overlay welding by the TIG process with cold wire feed. Weld Int 32(2): 130–138
21. Divya M, Albert SK (2018) Dilution effects on weld metal microstructure and liquation cracking susceptibility of 304B4 SS joined using E309 electrode. J Manuf Process 34:540–554
22. Westerbaan D, Parkes D, Nayak SS, Chen DL, Biro E, Goodwin F, Zhou Y (2014) Effects of concavity on tensile and fatigue properties in fibre laser welding of automotive steels. Sci Technol Weld Join 19(1):60–68
23. Liang Y, Shen J, Hu S, Wang H, Pang J (2018) Effect of TIG current on microstructural and mechanical properties of 6061-T6 aluminum alloy joints by TIG–CMT hybrid welding. J Mater Process Technol 255:161–174
24. Wang H, Jiang W, Ouyang J, Kovacevic R (2004) Rapid prototyping of 4043 Al-alloy parts by VP-GTAW. J Mater Process Technol 148(1):93–102
25. Chen CS, Yang JG, Tan AH (2009) Study of welding peak temperatures on microstructures and hardness of heat affected zone in 2024-T3 aluminum alloy. Mater Sci Technol 25(7):896–904

Publisher's note Springer Nature remains neutral with regard to jurisdictional claims in published maps and institutional affiliations.